



Sodium substitution for partial lithium to significantly enhance the cycling stability of Li_2MnO_3 cathode material

Xin Dong, Youlong Xu*, Lilong Xiong, Xiaofei Sun, Zhengwei Zhang

Electronic Materials Research Laboratory, Key Laboratory of the Ministry of Education & International Center for Dielectric Research, Xi'an Jiaotong University, Xi'an 710049, PR China

HIGHLIGHTS

- Na-substituted Li_2MnO_3 is prepared by a conventional solid state reaction.
- A high capacity retention of 98.6% after 100 cycles is obtained.
- The roles of partial phase transformation to spinel are studied.

ARTICLE INFO

Article history:

Received 25 March 2013

Received in revised form

14 May 2013

Accepted 30 May 2013

Available online 10 June 2013

Keywords:

Sodium substitution

Cycling stability

Lithium-rich manganese oxide

Phase transformation

Lithium-ion batteries

ABSTRACT

Monoclinic layered Li_2MnO_3 has been extensively investigated due to its large discharge capacity. However, the poor cycling stability hinders its application as a cathode material of lithium-ion batteries. Herein we present a new strategy of sodium substitution for partial lithium to significantly enhance the cycling stability of Li_2MnO_3 through a conventional solid state reaction. In the electrochemical window of 2.0–4.6 V vs. Li/Li^+ , $\text{Li}_{1.90}\text{Na}_{0.10}\text{MnO}_3$ delivers an initial discharge capacity of 181 mAh g^{-1} with an excellent capacity retention of 99.3% after 45 cycles at $1/10 \text{ C}$, and 161 mAh g^{-1} with a capacity retention of 98.6% after 100 cycles at $1/2 \text{ C}$. Sodium substitution for partial lithium is promising to make Li_2MnO_3 be practically applied at a low current density.

© 2013 Elsevier B.V. All rights reserved.

1. Introduction

Nowadays, monoclinic layered Li_2MnO_3 ($\text{Li}[\text{Li}_{1/3}\text{Mn}_{2/3}]\text{O}_2$) has been extensively investigated owing to its advantages such as high theoretical capacity (up to 459 mAh g^{-1}), low cost, non-toxic and environmental benignity compared with conventional commercial cathode material LiCoO_2 [1–7]. However, several issues, for instance, the poor cycling stability [1,2,8] and rate performance [9], gas generation [2,8,10,11], and low first coulombic efficiency (FCE) [2,12,13], hinder its application as a cathode material of lithium-ion batteries.

Recently, ion substitution for transition metal has been applied to improve the electrochemical property of Li_2MnO_3 . Kim et al. [14] prepared $\text{Li}_{1.296}\text{Ni}_{0.056}\text{Mn}_{0.648}\text{O}_2$ ($\text{Li}_{1.944}\text{Ni}_{0.084}\text{Mn}_{0.972}\text{O}_3$) by Ni doping which releases a discharge capacity of 192 mAh g^{-1} between

2.0 and 4.8 V vs. Li/Li^+ at 0.2 mA cm^{-2} . Tabuchi et al. [15] reported that Fe-substituted Li_2MnO_3 , $\text{Li}_{1+x}(\text{Fe}_y\text{Mn}_{1-y})_{1-x}\text{O}_2$ ($0 < x < 1/3$, $0.2 \leq y \leq 0.4$), shows a high initial discharge capacity ($240\text{--}300 \text{ mAh g}^{-1}$) between 1.5 V and 4.8 V, and about 78% of capacity is maintained after 20 cycles. Fe and Ni co-substituted Li_2MnO_3 , $\text{Li}_{1+x}[(\text{Fe}_{1/2}\text{Ni}_{1/2})_y\text{Mn}_{1-y}]_{1-x}\text{O}_2$ is also reported with a highest capacity retention of 81% after 20 cycles between 2.0 and 4.8 V [16]. Daisuke Mori et al. [17] reported that ruthenium-substituted Li_2MnO_3 , $\text{Li}_2\text{Mn}_{0.4}\text{Ru}_{0.6}\text{O}_3$, exhibits a discharge capacity of 192 mAh g^{-1} in the initial cycle and 169 mAh g^{-1} in the tenth cycle at $1/10 \text{ C}$. However, the modified electrochemical property attributed to transition element substitution, especially the cycling stability, is still far insufficient to satisfy the requirement of application.

In this work, we select alkali Na-substitution for partial Li to improve the electrochemical performance of Li_2MnO_3 . The cycling stability and rate performance of $\text{Li}_{2-x}\text{Na}_x\text{MnO}_3$ with different substitution amount ($0 \leq x \leq 0.20$) are discussed. In addition, the roles of Na-substitution in improving the electrochemical performance are investigated.

* Corresponding author. Tel./fax: +86 29 82665161.

E-mail address: ylxujtu@mail.xjtu.edu.cn (Y. Xu).

2. Experimental

Na-substituted lithium manganese oxide, $\text{Li}_{2-x}\text{Na}_x\text{MnO}_3$ ($x = 0.00, 0.02, 0.05, 0.10, 0.15$ and 0.20) was synthesized by a

conventional solid state reaction. Stoichiometric amounts of Li_2CO_3 , Na_2CO_3 and MnCO_3 as the raw materials were thoroughly mixed and then sintered in air for 8 h with intermediate grindings. The sintering temperature was selected at 400°C to obtain materials

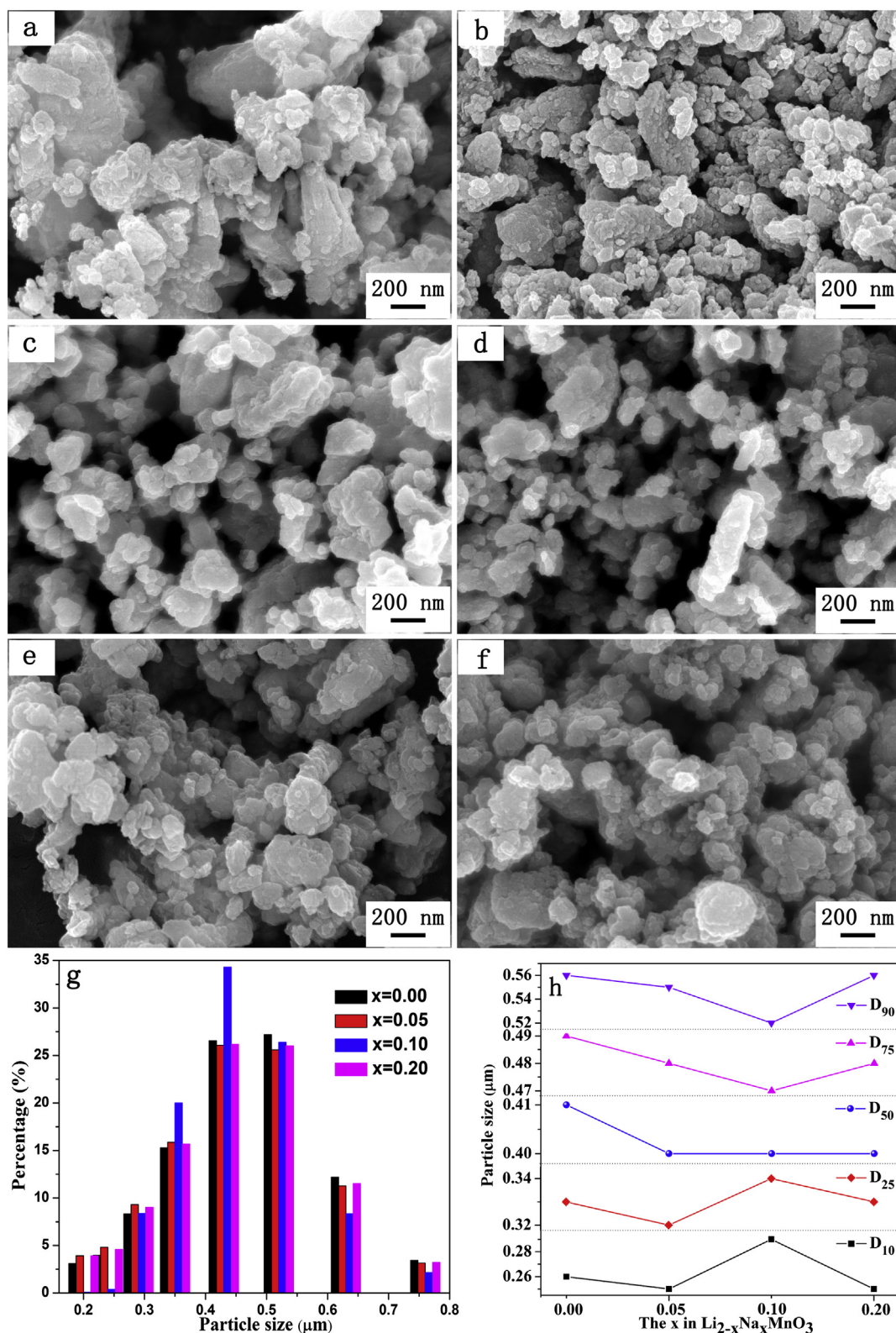


Fig. 1. The SEM images of $\text{Li}_{2-x}\text{Na}_x\text{MnO}_3$: a, $x = 0.00$, b, $x = 0.02$, c, $x = 0.05$, d, $x = 0.10$, e, $x = 0.15$ and f, $x = 0.20$. The particle size distribution of $\text{Li}_{2-x}\text{Na}_x\text{MnO}_3$ ($x = 0.00, 0.05, 0.10, 0.20$) is shown in g and h.

with small particle size and high surface area, which tend to provide high capacity and the rate property.

The powder X-ray diffraction (XRD) to characterize the crystal structure was performed on a PANalytical, X'Pert PRO diffractometer equipped with a Cu-K α radiation by step scanning for 2θ values in the range of 10° – 80° . The Fourier transform infrared absorption spectroscopies (FTIR) were recorded with a Fourier transform interferometer (BRUKER, TENSOR 27) in the wavenumber range of 400 – 4000 cm^{-1} at a spectral resolution of 2 cm^{-1} . The particle morphologies of the sample were investigated using a field Emission scanning electron microscope (SEM) (Hitachi S-4800) and a transmission electron microscopy (TEM) (JEOL, JEM-2100). The particle size distribution was measured by a laser particle size analyzer (OMEC, LS-pop (6)).

The valence state of Mn in $\text{Li}_{2-x}\text{Na}_x\text{MnO}_3$ was determined by X-ray photoelectron spectroscopy (XPS), which was performed with an Axis ultra spectrometer (Kratos) using Mono Al K α (1486.71 eV) radiation at a power of 225 W (15 mA , 15 kV). All data were calibrated against the C 1s peak at 284.6 eV .

The electrochemical impedance spectroscopy (EIS) and cyclic voltammetry (CV) measurements were tested using Versatile Multichannel Potentiostat 2/Z with the ability for impedance measurements (Bio-logic). Herein, the EIS was tested at open-circuit voltage (around 3.1 V vs. Li/Li^+) in the frequency range from 10 mHz to 100 kHz ; the CV was tested at different scan rates (from 0.1 to 1.0 mV s^{-1}) between 2.0 and 4.6 or 4.8 V .

Electrochemical performance of the sample was measured using CR2016 coin-type cell with lithium foil as the anode electrode. To fabricate the tested cathode electrode, the prepared active material was mixed with carbon black, and polyvinylidene fluoride binder (PVDF) in *N*-methyl-2-pyrrolidone (NMP) in the weight ratio of $70:20:10$ to form a slurry. Then this slurry was coated onto a roughened aluminum foil and dried at 120°C overnight in a vacuum condition oven to eliminate the NMP. The electrolyte is 1 M LiPF_6 dissolved in ethylene carbonate/diethyl carbonate/ethyl methyl carbonate with a $1:1:1$ volume ratio (CAPCHEM). The battery cells were assembled in argon-filled glove box (Mikrouna Super ($1225/750$)) with H_2O and O_2 concentrations below 0.1 ppm . All cells were charged and discharged at room temperature between 2.0 and 4.6 V vs. Li/Li^+ .

3. Results and discussion

The particle size, morphology and crystallinity are important to the electrochemical performance of the cathode material [18,19]. The surface morphology of the samples with different substitution content is investigated by SEM analysis and the results are shown in Fig. 1. All samples have agglomerated secondary particles which are composed of much smaller primary particles. The particle size

distribution of $\text{Li}_{2-x}\text{Na}_x\text{MnO}_3$ ($x = 0.00, 0.05, 0.10, 0.20$) measured by a laser particle size analyzer is shown in Fig. 1g and h. Most of the secondary particles of $\text{Li}_{1.90}\text{Na}_{0.10}\text{MnO}_3$ are mainly distributed around $0.4\text{ }\mu\text{m}$, and the D_{90} , D_{75} and D_{50} of $\text{Li}_{1.90}\text{Na}_{0.10}\text{MnO}_3$ are smaller while the D_{10} and D_{25} are larger than other samples. That is, the average particle size of $\text{Li}_{1.90}\text{Na}_{0.10}\text{MnO}_3$ is smaller and particle size distribution is more uniform.

TEM is performed to further study the morphology of the primary particles. Fig. 2 depicts the TEM images of Li_2MnO_3 and $\text{Li}_{1.90}\text{Na}_{0.10}\text{MnO}_3$, which are used as representatives. The size of the primary particles of Li_2MnO_3 is about 30 – 80 nm , while the size of $\text{Li}_{1.90}\text{Na}_{0.10}\text{MnO}_3$ is about 10 – 40 nm . Furthermore, the particles of $\text{Li}_{1.90}\text{Na}_{0.10}\text{MnO}_3$ are more regular and homogeneous than that of Li_2MnO_3 , as marked by red circles, which implies a higher crystallinity with a more stable crystalline structure. Combining the TEM and SEM, $\text{Li}_{1.90}\text{Na}_{0.10}\text{MnO}_3$ possesses smaller particle sizes and a higher crystallinity, which are beneficial to Li-ion transport and the cycling stability of cathode material.

The X-ray diffraction patterns of $\text{Li}_{2-x}\text{Na}_x\text{MnO}_3$ are shown in Fig. 3. All diffraction peaks are broadening, which are attributed to the poor crystallinity obtained at the low synthesis temperature [20]. Na-substituted samples exhibit similar diffraction patterns to Li_2MnO_3 , which can all be indexed into O3-type monoclinic layer structure with a space group of C2/m . With the increase of x , the diffraction peaks, such as (130) , (-132) and (330) , shift to lower angles, suggesting that Na-ions insert into the crystal structure and simultaneously change the lattice parameters. Meanwhile, the characteristic superlattice peaks of Li_2MnO_3 between 20 and 25° (2θ) become weaker, as shown in Fig. 3c, indicating that Na-ions enter the transition metal (TM) layer and as a result demolish the local ordered distribution of Li/Mn with a ratio of $1:2$. In addition, the peak around 65° (2θ) splits into two peaks, (-133) and (-331) , which can be only indexed to C2/m space group with higher crystallinity [20]. This phenomenon reveals that Na-substitution enhances the crystallinity of material, which is consistent with the result from TEM.

For $x \leq 0.10$ samples, the rather obvious shift of (001) to lower angles, as shown in Fig. 3b, demonstrates that Na-ions broaden the space for Li-ion migration in the host structure [21]. In contrast, when $x \geq 0.15$, the peaks (001) , (-131) and (131) shift to higher angles, suggesting a slight shrink of the unit cell volume. Furthermore, $\text{Li}_{2-x}\text{Na}_x\text{MnO}_3$ ($x \geq 0.15$) possesses additional impure peak at 56.2° (2θ), which can be indexed into $\text{Na}_2\text{Mn}_3\text{O}_7$ (Ref. code: 01-078-0193). And more $\text{Na}_2\text{Mn}_3\text{O}_7$ is formed with more substitution amount, as shown in the inset of Fig. 3a.

Fig. 4 shows the X-ray photoelectron spectroscopy (XPS) of Mn 2p of $\text{Li}_{2-x}\text{Na}_x\text{MnO}_3$. The binding energies of Mn $2p_{3/2}$ and $2p_{1/2}$ in Li_2MnO_3 are 642.6 and 654.2 eV with a binding energy splitting of 11.6 eV , which demonstrate that the valence of Mn in Li_2MnO_3 is

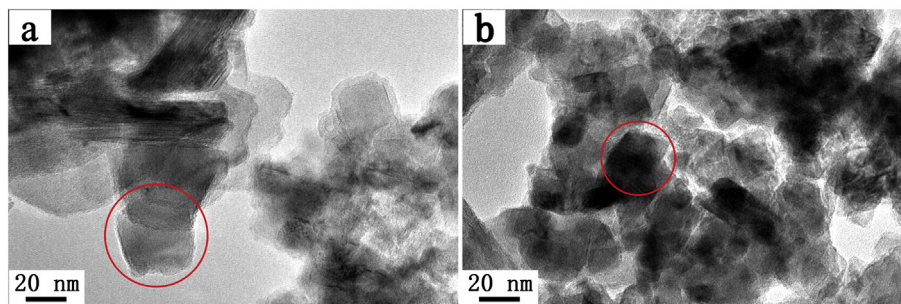


Fig. 2. The TEM images of Li_2MnO_3 (a) and $\text{Li}_{1.90}\text{Na}_{0.10}\text{MnO}_3$ (b). One single grain is circled by a red circle. (For interpretation of the references to colour in this figure legend, the reader is referred to the web version of this article.)

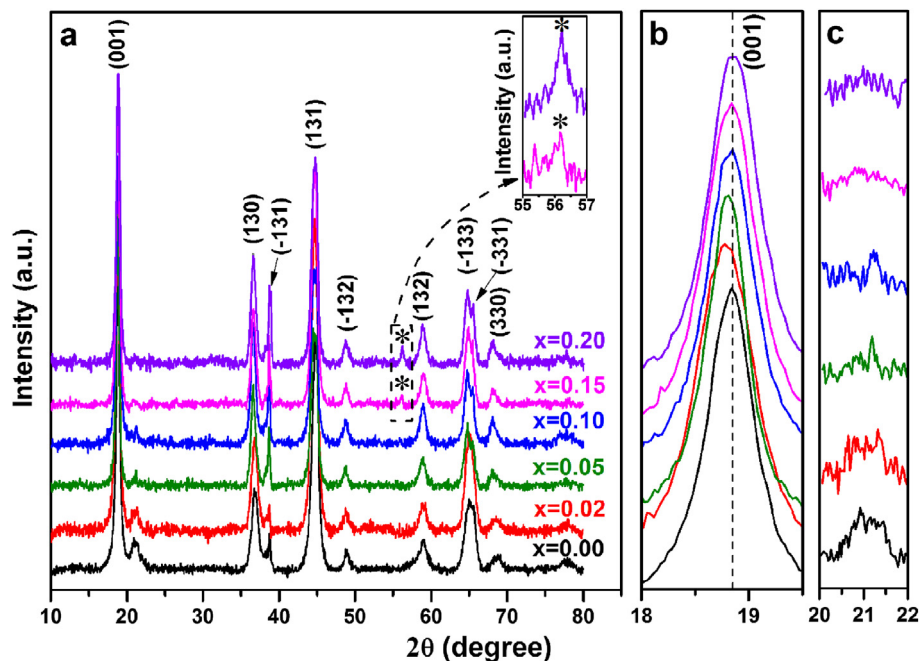


Fig. 3. X-Ray diffraction patterns of $\text{Li}_{2-x}\text{Na}_x\text{MnO}_3$ ($x = 0.00, 0.02, 0.05, 0.10, 0.15$ and 0.20). The reflection peak (001) and the peaks around 21° (2θ) which correspond to the superlattices are magnified and shown in b and c, respectively. The patterns in dotted box and the asterisks “*” in a indicate reflection peaks associated with impure phase $\text{Na}_2\text{Mn}_2\text{O}_7$, which are also magnified and shown in the inset of a.

tetravalent [22]. After Na-substitution, the peaks of $2p_{3/2}$ shift to lower energy accompanied with shoulders appear at slightly higher binding energies, while $2p_{1/2}$ show negligible changes both in shape and position. These phenomena indicate that Na-substitution leads to a certain amount of Mn with lower valence state generated in Na-substituted samples. The valence of Mn in $\text{Na}_2\text{Mn}_2\text{O}_7$ is fully tetravalent; consequently, it means that new Li–Mn–O phase with lower valence Mn-ion is formed in $\text{Li}_{2-x}\text{Na}_x\text{MnO}_3$.

The effects of Na-substitution on the electrochemical properties of $\text{Li}_{2-x}\text{Na}_x\text{MnO}_3$ were characterized. Fig. 5 shows the initial

charge–discharge curves of samples with different x . The tests were performed at a considerably low current density of $1/30$ C to reveal the essential charge–discharge performance.

Above 4.4 V, a characteristic charge plateau is observed for every sample, which is related to simultaneous removal of lithium- and oxygen-ions from the crystal without any change to the tetravalent oxidation state of Mn-ions [2–4,10,23–26]. In contrast to pristine Li_2MnO_3 , Na-substituted samples possess additional charge plateau at about 4.15 V and prominent discharge plateau at about 4.1 and 2.8 V. These three plateaus are the characteristic plateaus of spinel LiMn_2O_4 , in which the charge/discharge plateau around 4.1 V is

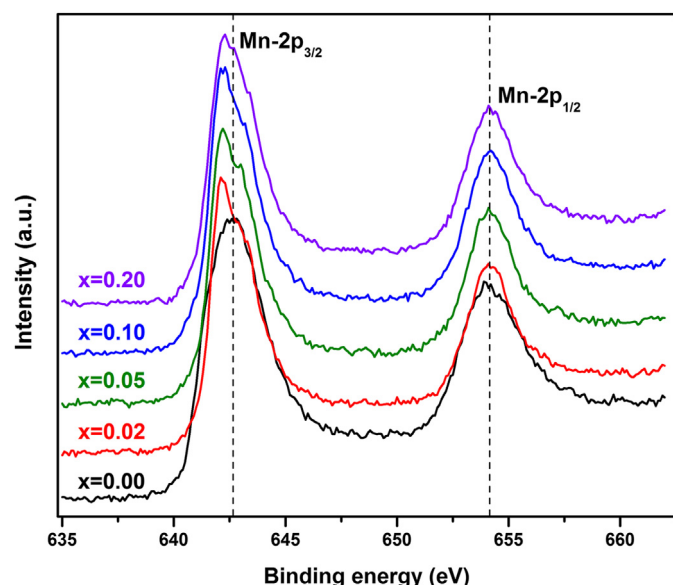


Fig. 4. The XPS spectra of Mn 2p of $\text{Li}_{2-x}\text{Na}_x\text{MnO}_3$ ($x = 0.00, 0.02, 0.05, 0.10$ and 0.20).

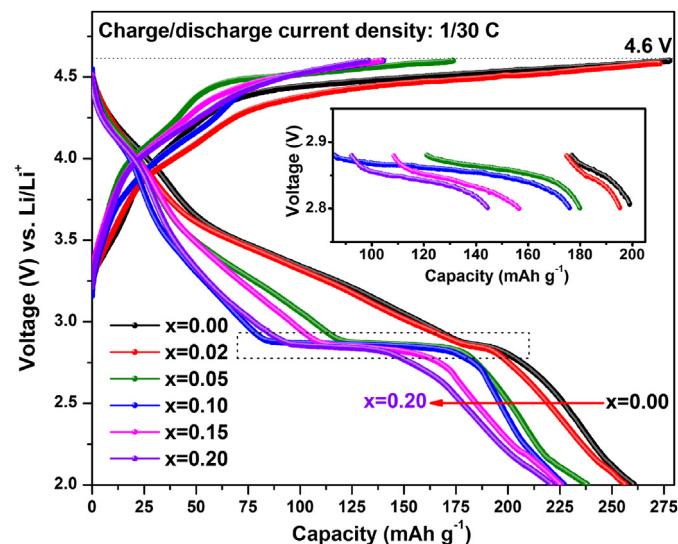


Fig. 5. The initial charge/discharge curves of $\text{Li}_{2-x}\text{Na}_x\text{MnO}_3$ ($x = 0.00, 0.02, 0.05, 0.10, 0.15$ and 0.20) obtained at $1/30$ C. The plateaus around 2.8 V are expanded and shown in the inset.

related to the de-intercalation/intercalation of Li-ions from/into Li–O tetrahedral sites while the plateau at 2.8 V is associated with the intercalation into octahedral sites in the spinel structure [1,27]. The charge plateau above 4.4 V decreases while the plateaus around 4.1 and 2.8 V lengthen after Na-substitution, which indicate that Na-substitution restrains the release of oxygen and induces the spinel phase generated during the sintering process. In addition, the noteworthy discharge plateau around 2.8 V, which lacks corresponding charge plateaus, suggests a remarkable structure change occurring in $\text{Li}_{2-x}\text{Na}_x\text{MnO}_3$ (especially for $x = 0.10$) in the initial charge.

From Fig. 5, the discharge capacity becomes larger than the charge capacity for the samples $x > 0.02$, which means more Li-ions are intercalated into the oxide than those extracted. These excess Li-ions are speculated to be inserted into vacant octahedral sites, which may be engendered after the initial charge. The original Mn and Li-ions in Li_2MnO_3 all occupy octahedral sites. In the initial charge, when the Li-ion content is reduced to a certain value of about 50%, Mn-ions would migrate from octahedral sites in TM layer to tetrahedral sites in the neighboring Li layer. Meanwhile, Li-ions may be allowed to migrate from their octahedral sites, through a shared face, into neighboring tetrahedral sites in Li layer [28]. Following such displacement, vacant octahedral sites are generated in TM layer and Li layer, which may accommodate the excess Li-ions.

The initial discharge capacity at 1/30 C of $\text{Li}_{2-x}\text{Na}_x\text{MnO}_3$ is also shown in Table 1. The sample $x \leq 0.05$ releases a capacity $>238 \text{ mAh g}^{-1}$, in which approximately 229 mAh g^{-1} can be accounted for by the reduction of Mn^{4+} to Mn^{3+} [1,2,3]. The remaining charge compensation may be ascribed to the exchange between Li^+ and H^+ originating from electrolyte decomposition [2,4,5] or the partial oxidation of O^{2-} anions [21]. When $x \geq 0.10$, however, the discharge capacity become smaller than 229 mAh g^{-1} . The variation may be attributed to the decrease of oxygen release in the initial charge, which would restrain the reactions involving electrolyte decomposition and the oxidation of O^{2-} . Although the discharge capacity is sacrificed somewhat after Na-substitution, the accompanying decrease of oxygen evolution could reduce the side reactions involving oxygen and improve the structural stability, which are beneficial to the cycling stability of Li_2MnO_3 .

To investigate the effect of Na-substitution on the cycle performance of Li_2MnO_3 , the half-cells were charged/discharged at a moderate current density of 1/10 C and 1/2 C, as depicted in Fig. 6 and Table 1. Na-substitution with appropriate amount could improve the cycle performance of Li_2MnO_3 . For example, $\text{Li}_{1.90}\text{Na}_{0.10}\text{MnO}_3$ delivers an initial discharge capacity of 181 mAh g^{-1} at 1/10 C with a capacity retention of 99.3% after 45 cycles, while pristine Li_2MnO_3 only exhibits a retention of 60.3%. Increasing the current density to 1/2 C, $\text{Li}_{1.90}\text{Na}_{0.10}\text{MnO}_3$ similarly

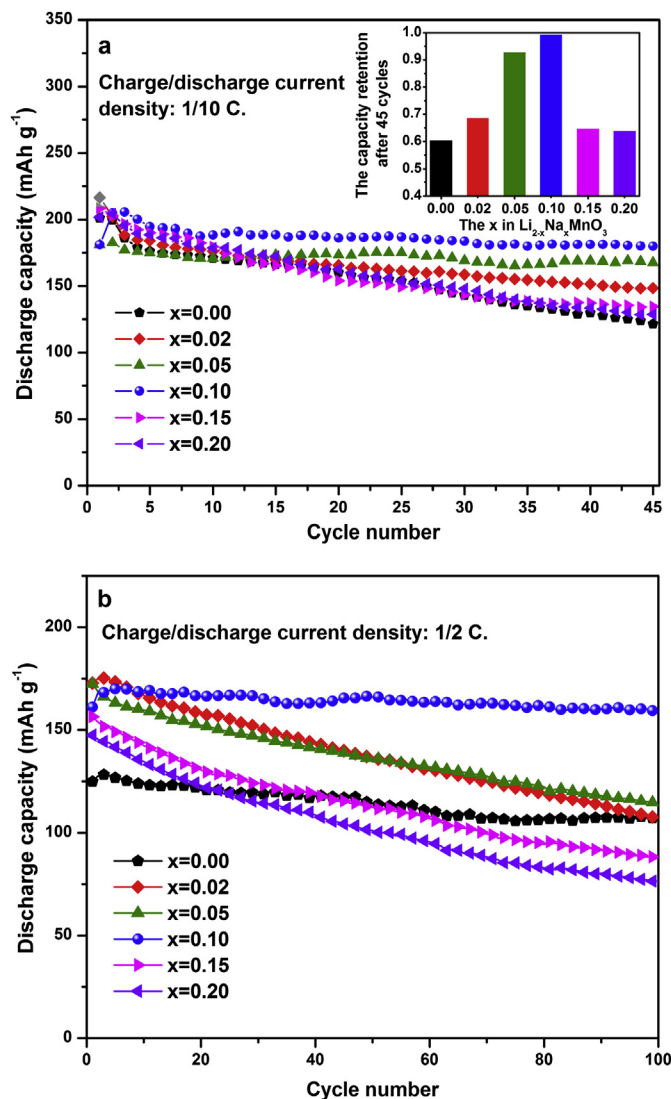


Fig. 6. The cycle performance of $\text{Li}_{2-x}\text{Na}_x\text{MnO}_3$ ($x = 0.00, 0.02, 0.05, 0.10, 0.15$ and 0.20) obtained at 1/10 C (a) and 1/2 C (b). The inset in a shows the capacity retention of $\text{Li}_{2-x}\text{Na}_x\text{MnO}_3$ after 45 cycles.

shows the highest capacity retention of 98.6% with a largest discharge capacity of 158.8 mAh g^{-1} after 100 cycles, while Li_2MnO_3 only delivers 106.2 mAh g^{-1} with a retention of 85.0%. It has been reported that O_2 evolution from Li_2MnO_3 could trigger a drastic volume reduction and structural deformation when half of

Table 1

The electrochemical properties of $\text{Li}_{2-x}\text{Na}_x\text{MnO}_3$ ($x = 0.00, 0.02, 0.05, 0.10, 0.15, 0.20$).

| Samples | $x = 0.00$ | $x = 0.02$ | $x = 0.05$ | $x = 0.10$ | $x = 0.15$ | $x = 0.20$ |
|--|------------|------------|------------|------------|------------|------------|
| Q_{1d} at 1/30 C (mAh g^{-1}) | 260.8 | 256.9 | 238.3 | 227.1 | 225.6 | 221.5 |
| Q_{1d} at 1/10 C (mAh g^{-1}) | 201.0 | 216.6 | 180.9 | 181.0 | 208.5 | 201.6 |
| Q_{45d} at 1/10 C (mAh g^{-1}) | 121.3 | 148.5 | 167.5 | 179.8 | 134.8 | 128.7 |
| R_{45} at 1/10 C | 0.603 | 0.685 | 0.926 | 0.993 | 0.646 | 0.638 |
| Q_{1d} at 1/2 C (mAh g^{-1}) | 124.9 | 172.8 | 172.4 | 161.1 | 156.4 | 147.5 |
| Q_{100d} at 1/2 C (mAh g^{-1}) | 106.2 | 107.2 | 114.8 | 158.8 | 88.3 | 76.4 |
| R_{100} 1/2 C | 0.850 | 0.620 | 0.666 | 0.986 | 0.565 | 0.518 |
| $Q_{1/20 \text{ C}}$ (mAh g^{-1}) | 219.9 | 233.0 | 220.6 | 212.8 | 223.0 | 217.9 |
| $Q_{1 \text{ C}}$ (mAh g^{-1}) | 80.4 | 139.2 | 123.7 | 140.6 | 109 | 104.1 |
| $Q_{1 \text{ C}}/Q_{1/20 \text{ C}}$ | 0.366 | 0.597 | 0.561 | 0.661 | 0.489 | 0.478 |

Q_{1d} , the initial discharge capacity; Q_{45d} , Q_{100d} , the discharge capacity in the 45th cycle and in the 100th cycle; R_{45} , R_{100} , the capacity retention after 45 cycles and 100 cycles, respectively; $Q_{1/20 \text{ C}}$, $Q_{1 \text{ C}}$, the discharge capacity at 1/20 C and 1 C, respectively.

Li-ions are extracted, which in turn leads to a poor cyclability [8]. Consequently, the improved cycle performance attributed to Na-substitution ($x \leq 0.10$) could be partly attributed to the stable structure since less oxygen is released from the host structure in the initial charge process. However, excess substitution ($x \geq 0.15$) leads to deteriorated cycle performance, which may be related to the newborn $\text{Na}_2\text{Mn}_3\text{O}_7$ phase. The generation of $\text{Na}_2\text{Mn}_3\text{O}_7$ could lead to the segregation of Mn-ions from $\text{Li}_{2-x}\text{Na}_x\text{MnO}_3$ due to the higher molar ratio of Mn/Na in $\text{Na}_2\text{Mn}_3\text{O}_7$ than Mn/Li ratio in Li_2MnO_3 . The segregation of Mn-ions would result in the degradation of structural stability and the shrink of unit cell, which are unfavorable for the cycling stability and Li-ion diffusion.

The charge/discharge curves of Li_2MnO_3 and $\text{Li}_{1.90}\text{Na}_{0.10}\text{MnO}_3$ in the first cycle and in the 100th cycle at 1/2 C are shown in Fig. 7. Similar to the curve in the first cycle, Li_2MnO_3 has no distinguishable plateau around 4.1 V after 100 cycles, which suggests no evident phase transition occurred in Li_2MnO_3 along with cycle. However, the charge/discharge plateau for $\text{Li}_{1.90}\text{Na}_{0.10}\text{MnO}_3$ becomes much longer with distinct dividing into two plateaus after 100 cycles, suggesting more spinel phase generated with cycle. Attributed to the phase transformation, the discharge energy density of $\text{Li}_{1.90}\text{Na}_{0.10}\text{MnO}_3$, which is calculated by integrating the voltage over the specific capacity, increases from 464.0 Wh kg^{-1} to 486.5 Wh kg^{-1} , while the energy density of Li_2MnO_3 decreases from 400.1 Wh kg^{-1} to 334.3 Wh kg^{-1} after 100 cycles.

Fig. 8 shows the discharge capacity of $\text{Li}_{2-x}\text{Na}_x\text{MnO}_3$ as a function of C-rates ranging from 1/20 C to 1 C (1/20 C corresponds to 10 mA g^{-1}) to study the role of Na-substitution in improving the rate capability of Li_2MnO_3 . At a lower current density of 1/20 C, all samples exhibit similar discharge behavior, which is due to the low enough current density to allow practically all possible Li-ions to be inserted and extracted. With the increase of the current density, Na-substituted samples show more preferable rate performance than Li_2MnO_3 . From the inset of Fig. 8, it's observed that, the rate performance improves first ($x \leq 0.10$) and then deteriorates with the increase of x , which is similar to the cycle performance. It is noted that $\text{Li}_{1.90}\text{Na}_{0.10}\text{MnO}_3$ demonstrates the largest discharge capacity of 140.6 mAh g^{-1} at 1 C, which is almost twice as that of Li_2MnO_3 (80.4 mAh g^{-1}). Moreover, when the rate is reduced from 1 C to 1/10 C, $\text{Li}_{1.90}\text{Na}_{0.10}\text{MnO}_3$ shows a little capacity fade of 3.7% while Li_2MnO_3 delivers 9.6% capacity fade of the seventh cycle at the same rate, which implies that Na-substitution ($x = 0.10$) markedly enhances the rate performance and the reversibility of Li_2MnO_3 undergoing a high current density.

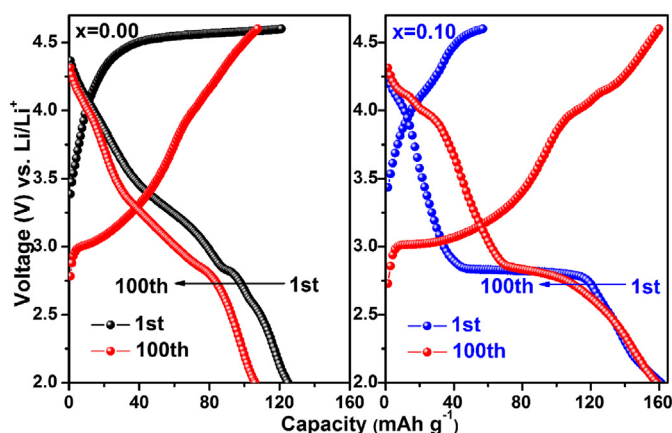


Fig. 7. The charge–discharge curves of $\text{Li}_{2-x}\text{Na}_x\text{MnO}_3$ ($x = 0.00$ and 0.10) in 1st cycle and 100th cycle, respectively.

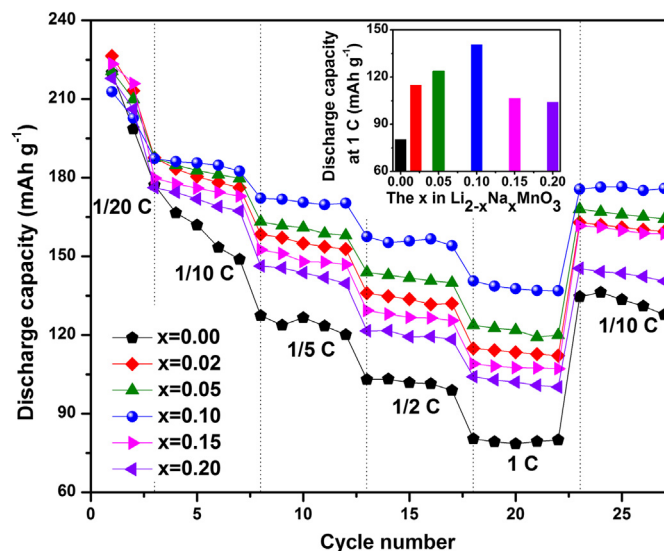


Fig. 8. The rate performance of $\text{Li}_{2-x}\text{Na}_x\text{MnO}_3$ ($x = 0.00, 0.02, 0.05, 0.10, 0.15$ and 0.20). The current density increases from 1/20 C to 1 C and then decreases to 1/10 C. The discharge capacity at 1 C is shown in the inset.

Pure Li_2MnO_3 shows relatively poor capacity stability and rate performance. Therefore, the most appreciated cycle stability and rate performance delivered by $\text{Li}_{1.90}\text{Na}_{0.10}\text{MnO}_3$ is particularly noteworthy, as it illustrates that a small amount of Na-substitution is sufficient to improve the electrochemical performance of Li_2MnO_3 . Consequently, we select $\text{Li}_{1.90}\text{Na}_{0.10}\text{MnO}_3$ in subsequent studies to investigate the mechanism of Na-substitution to enhance the electrochemical property of Li_2MnO_3 .

To clarify the structure changes after cycles, the XRD profiles of Li_2MnO_3 and $\text{Li}_{1.90}\text{Na}_{0.10}\text{MnO}_3$ before and after 100 cycles are shown in Fig. 9. Both samples exhibit similar diffraction patterns before and after cycle, except for the degradation of peak (001) and the noticeable newborn diffraction peaks at 25.3° (2θ), which can be indexed to LiMnO_2 . The appearance of LiMnO_2 suggests the discharge process of Li_2MnO_3 involving the reduction of Mn^{4+} to

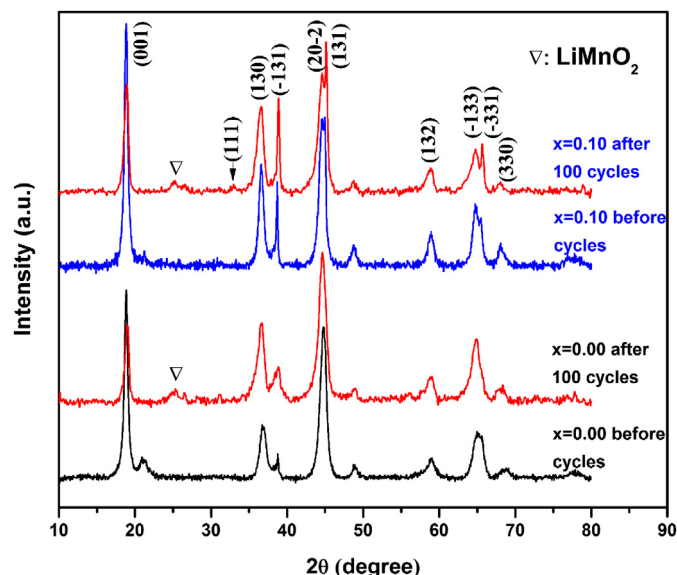


Fig. 9. The XRD patterns of $\text{Li}_{2-x}\text{Na}_x\text{MnO}_3$ ($x = 0.00$ and 0.10) before and after 100 cycles. The triangle in the pattern corresponds to LiMnO_2 .

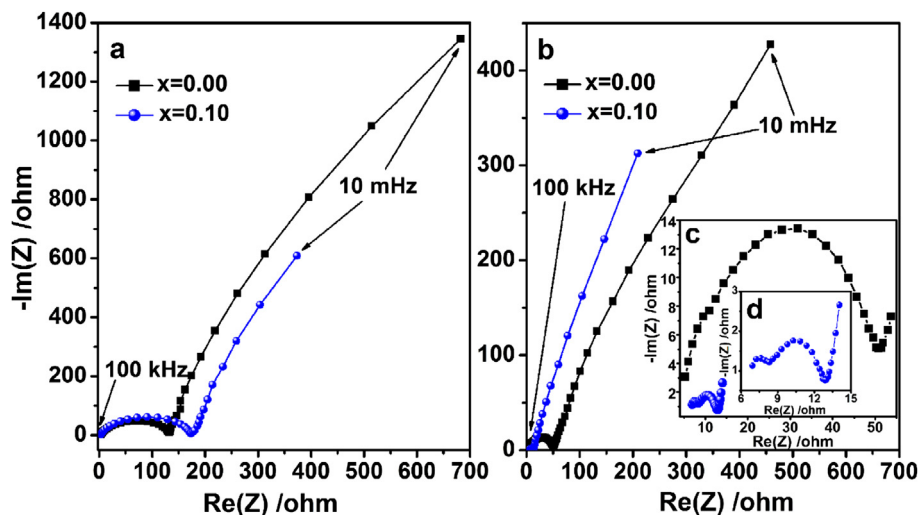


Fig. 10. The electrochemical impedance spectroscopy (EIS) of $\text{Li}_{2-x}\text{Na}_x\text{MnO}_3$ ($x = 0.00$ and 0.10). a, before cycle; b, after 11 cycles. The high frequency regions of EIS after cycle are local magnified, as shown in c and d.

Mn^{3+} . For Li_2MnO_3 , the superlattice peaks around 20° (2θ) disappear as well as the peaks (130), (131), (-331) and (330) shift to lower angles after cycle. The disappearance of the superlattices is attributed to the removal of Li-ions from TM layer, while the peak shift suggests evident volume change after cycle. In contrast, $\text{Li}_{1.90}\text{Na}_{0.10}\text{MnO}_3$ does not show such obvious changes. Moreover, the peaks around 45° and 65° (2θ) of $\text{Li}_{1.90}\text{Na}_{0.10}\text{MnO}_3$ are split more distinctly after 100 cycles. These observations indicate that $\text{Li}_{1.90}\text{Na}_{0.10}\text{MnO}_3$ exhibits more appreciated structure stability compared with pristine Li_2MnO_3 during cycle, which is significant to the cycling stability of the electrode material.

The electrochemical performance of the electrode material highly depends on the kinetic properties, such as the charge transfer reaction at the electrolyte/electrode interface and the Li-ion diffusion coefficient in the host structure [29]. Fig. 10 shows the EIS of $\text{Li}_{2-x}\text{Na}_x\text{MnO}_3$ ($x = 0.00$ and 0.10) before and after 11 cycles, respectively. $\text{Li}_{1.90}\text{Na}_{0.10}\text{MnO}_3$ shows a slightly larger charge transfer resistance (R_{ct}) (174.4 Ω) than Li_2MnO_3 (133.3 Ω) before cycle. However, the R_{ct} of $\text{Li}_{1.90}\text{Na}_{0.10}\text{MnO}_3$ becomes obviously smaller (12.7 Ω) than Li_2MnO_3 (50.8 Ω) after 11 cycles, which

indicates that Na-substitution facilitates electron transport at the interface between the electrode and electrolyte in subsequent cycles. Herein the decrease of R_{ct} after cycle is due to the release of oxygen and the modification of surface structure associated with lattice rearrangement after the initial charge [11,28].

The Li-ion diffusion coefficients in Li_2MnO_3 and $\text{Li}_{1.90}\text{Na}_{0.10}\text{MnO}_3$ are also studied to further investigate the impact of Na-substitution on the kinetic properties. Fig. 11 shows the cyclic voltammograms of Li_2MnO_3 and $\text{Li}_{1.90}\text{Na}_{0.10}\text{MnO}_3$ after the first cycle under different scan rates ($0.1\text{--}1.0\text{ mV s}^{-1}$). With the increase of the scan rate (v), the magnitude of peak current (I_p) increases as well as the cathodic and anodic peaks move to lower and higher voltages, respectively. Assuming a semi-infinite and finite diffusion of Li-ion in solid thin film and the rate of electron transfer at the interface between electrolyte and electrode is fast enough, the relationship of I_p and v can be described by the following equation:

$$I_p = (2.69 \times 10^5) n^{3/2} D^{1/2} v^{1/2} SC$$

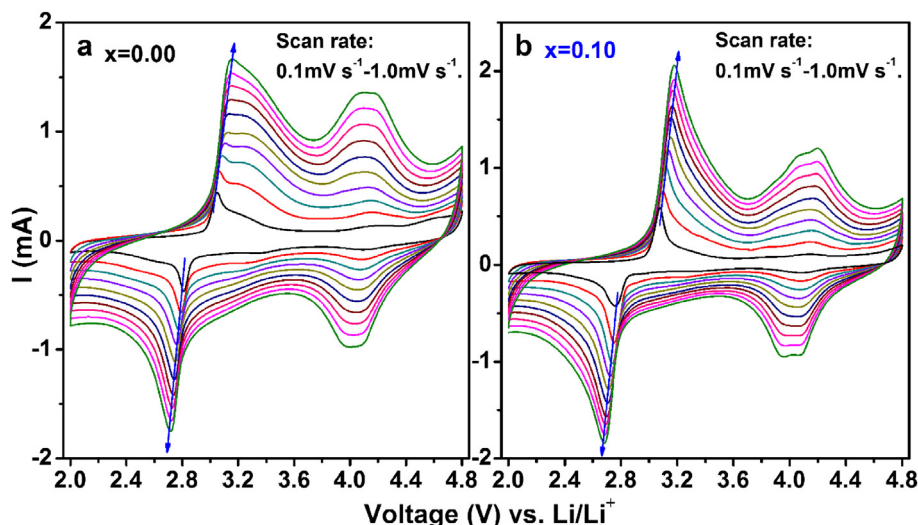


Fig. 11. The cyclic voltammograms (CV) of Li_2MnO_3 (a) and $\text{Li}_{1.90}\text{Na}_{0.10}\text{MnO}_3$ (b) at various scan rates (from 0.1 mV s^{-1} to 1.0 mV s^{-1} with an interval of 0.1 mV s^{-1}).

where I_p is the peak current, n is the number of electrons for per reaction species, D is the Li-ion diffusion coefficient in the electrode, v is the potential scan rate, S is the electrode area, and C is the bulk concentration of Li-ion in the electrode [30,31]. Assuming that the film of the electrode is a compact uniform layer, the diffusion coefficient can be calculated from the linear relationship between the square of peak currents and the scan rates according to the equation. The uppermost redox couple locates at 3.1/2.8 V, consequently, we choose to study the diffusion coefficient at about 3.1/2.8 V. In this case, the relationships between I_p^2 and v at 3.1 and 2.8 V are shown in Fig. 12. Calculated from the slopes of the linear fit, the diffusion coefficient in Li_2MnO_3 at 3.1/2.8 V is $2.684 \times 10^{-13}/2.994 \times 10^{-13} \text{ cm}^2 \text{ s}^{-1}$; while $\text{Li}_{1.90}\text{Na}_{0.10}\text{MnO}_3$ displays a higher Li-ion diffusion coefficient of $5.612 \times 10^{-13}/4.6748 \times 10^{-13} \text{ cm}^2 \text{ s}^{-1}$, respectively. The diffusion coefficient in $\text{Li}_{1.90}\text{Na}_{0.10}\text{MnO}_3$ is about twice that of Li_2MnO_3 , indicating that Na-substitution is conducive to Li-ion transport in the host structure. As a consequence, it's considered that the increased Li-ion diffusion coefficient and the decreased charge transfer resistance account for the enhanced cycling stability and rate performance of $\text{Li}_{1.90}\text{Na}_{0.10}\text{MnO}_3$.

Fig. 13 shows the cyclic voltammograms (CV) of Li_2MnO_3 and $\text{Li}_{1.90}\text{Na}_{0.10}\text{MnO}_3$ performed at a scan rate of 0.1 mV s^{-1} . In contrast to Li_2MnO_3 , $\text{Li}_{1.90}\text{Na}_{0.10}\text{MnO}_3$ has an obvious peak around 4.1 V in the initial oxidation process, which suggests that some spinel phase has been formed in $\text{Li}_{1.90}\text{Na}_{0.10}\text{MnO}_3$ during the sintering process.

Nevertheless, there is no pronounced characteristic peaks of spinel phase can be distinguished in the XRD patterns of Na-substituted samples, which may be attributed to the low amount and the discrete local distribution of the spinel phase in the composite. Instead, FTIR spectroscopy is convenient and powerful local probes for the structural evaluation of Lithium manganese oxide [32]. Fig. 14 shows the FTIR spectroscopy of $\text{Li}_{2-x}\text{Na}_x\text{MnO}_3$ ($x = 0.00, 0.05, 0.10, 0.20$) between 400 and 800 cm^{-1} . There are four dominant absorption bands for Li_2MnO_3 locating at approximately 631, 540, 457 and 426 cm^{-1} , respectively. After Na-substitution, the band at 631 cm^{-1} shifts to higher wavenumber while the band at 540 cm^{-1} shifts to lower wavenumber, suggesting that the local environment of Mn–O is changed. Meanwhile, the low-wavenumber bands at 457 and 426 cm^{-1} , which are absent from the spinel phase, become much weaker. Furthermore, Na-substituted sample, especially $\text{Li}_{1.90}\text{Na}_{0.10}\text{MnO}_3$, possesses an additional band at 612 cm^{-1} , which is the characteristic band of spinel LiMn_2O_4 [32]. Therefore, it's believed that the spinel phase is indeed generated in Na-substituted samples.

To further study the phase transformation during cycle, the CV of Li_2MnO_3 and $\text{Li}_{1.90}\text{Na}_{0.10}\text{MnO}_3$ were performed at 0.2 mV s^{-1}

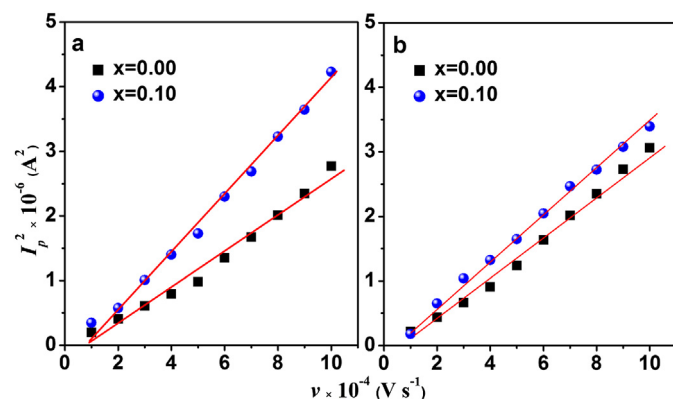


Fig. 12. Plots of the square of peak current (I_p^2) of the cyclic voltammograms vs. scan rate v . Plot a corresponds to the anodic peaks at 3.1 V and plot b corresponds to the cathodic peaks at 2.8 V.

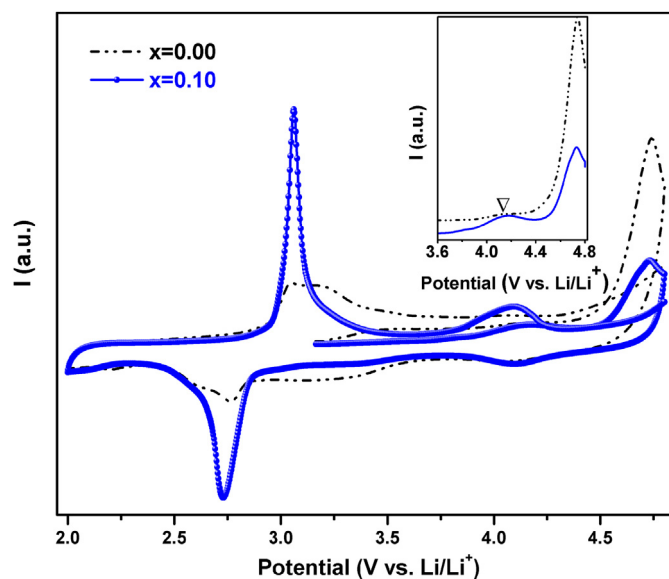


Fig. 13. The cyclic voltammograms of $\text{Li}_{2-x}\text{Na}_x\text{MnO}_3$ ($x = 0.00$ and 0.10) at a scan rate of 0.1 mV s^{-1} . The inset shows the local magnified pattern between 3.6 and 4.8 V in the first oxidation process.

between 2.0 and 4.6 V, and the regions around 4 V are magnified and shown in Fig. 15. The redox peaks of Li_2MnO_3 are weak and relatively stable; while the peaks of $\text{Li}_{1.90}\text{Na}_{0.10}\text{MnO}_3$ become more intense and divide into double peaks after cycles, which illustrate that more spinel phase is generated in $\text{Li}_{1.90}\text{Na}_{0.10}\text{MnO}_3$ along with cycle.

The cubic close-packing spinel structure is more stable than layered rock-salt Li_2MnO_3 , and provides a much higher diffusion coefficient of $3.5 \times 10^{-11} \text{ cm}^2 \text{ s}^{-1}$ due to the three-dimensional Li-ion diffusion channel [31]. Moreover, it has been reported that the occupancy of octahedral sites in spinel structure by one type of metal at different valences (Mn^{4+} and Mn^{3+}) promotes the migration of polarons [33,34]. Consequently, it is speculated that a certain amount of spinel phase induced by Na-ions serves to

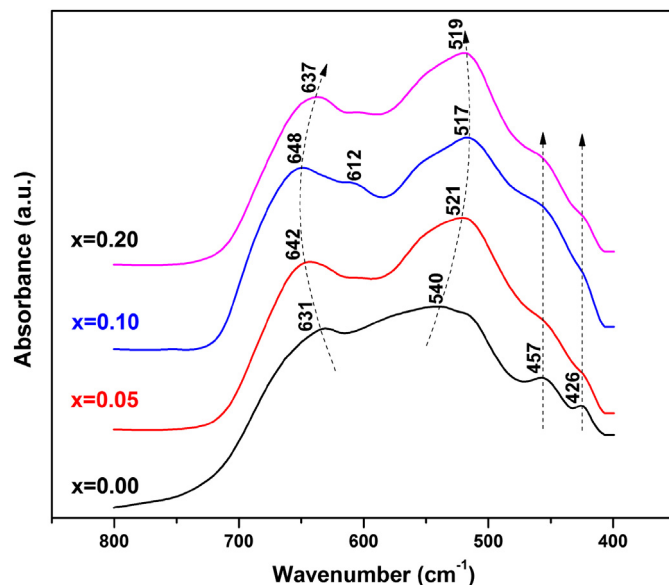


Fig. 14. The FTIR spectroscopy of $\text{Li}_{2-x}\text{Na}_x\text{MnO}_3$ ($x = 0.00, 0.05, 0.10, 0.20$) between 400 and 800 cm^{-1} .

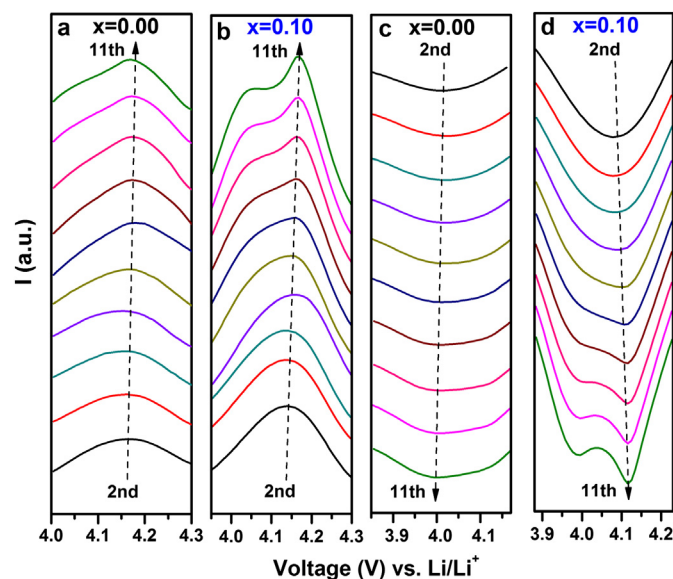


Fig. 15. The local magnified images (around 4 V) of CV profiles from 2nd cycle to 11th cycle of $\text{Li}_{2-x}\text{Na}_x\text{MnO}_3$ ($x = 0.00$ and 0.10) with a scan rate of 0.2 mV s^{-1} . Herein a and b correspond to anodic peaks of Li_2MnO_3 and $\text{Li}_{1.90}\text{Na}_{0.10}\text{MnO}_3$; c and d correspond to cathodic peaks of Li_2MnO_3 and $\text{Li}_{1.90}\text{Na}_{0.10}\text{MnO}_3$, respectively.

enhance the structure stability and facilitate Li-ion transport [35,36], which and then improves the cycling stability and rate performance of Li_2MnO_3 .

As mentioned above, Na-ion acts as a catalyst to promote the phase transformation to spinel, which plays important roles in the cycling stability and rate performance of Li_2MnO_3 . Herein, Rietveld refinement applied to XRD pattern is used to study the local structure of $\text{Li}_{1.90}\text{Na}_{0.10}\text{MnO}_3$, which may be useful to explore the effects of Na-substitution on the phase transformation. The calculated structural properties are shown in Table 2 and Fig. 16. The chemical formula of $\text{Li}_{1.90}\text{Na}_{0.10}\text{MnO}_3$ can be described as $[\text{Li}_{1.000}\text{Li}_{0.500}(\text{Li}_{0.231}\text{Mn}_{0.174}\text{Na}_{0.095})](\text{Mn}_{0.826}\text{Li}_{0.174})(\text{O}_{0.916}\text{O}_{1.855})$. It is noteworthy that approximately 7.6% oxygen vacancy is generated in $\text{Li}_{1.90}\text{Na}_{0.10}\text{MnO}_3$, which is attributed to the generation of spinel phase with lower valence Mn; and the oxygen vacancy may result in a higher conductivity and activate the Mn sites as the redox center in the lithium extraction process [8]. In addition, it is conjectured that the Na-ions, which mostly occupy Li 2b site, could maintain the structure stability when most of the Li-ions in 2b sites migrate to adjacent Li layer during the charge process. Furthermore, Na-ions may impel the migration of Mn-ions to adjacent Li layer, and as a result, induce the formation of the spinel phase [28,37]. However, this argument still needs further investigation in order to clarify the mechanism of phase transformation occurring in the crystal structure.

Table 2

Rietveld refinement results of $\text{Li}_{1.90}\text{Na}_{0.10}\text{MnO}_3$. $a = 4.985 \text{ \AA}$, $b = 8.521 \text{ \AA}$, $c = 4.990 \text{ \AA}$, $V = 199.855 \text{ \AA}^3$, $\beta = 109.45^\circ$.

| Atom | Site | Amount | x | y | z |
|--------|------|--------|---------|---------|---------|
| Li (1) | 4h | 1.000 | 0 | 0.65350 | 0.50000 |
| Li (2) | 2c | 0.500 | 0 | 0 | 0.50000 |
| Li (3) | 2b | 0.231 | 0 | 0.50000 | 0 |
| Na | | 0.095 | 0 | 0.50000 | 0 |
| Mn (1) | | 0.174 | 0 | 0.50000 | 0 |
| Mn (2) | 4g | 0.826 | 0 | 0.16795 | 0 |
| Li (4) | | 0.174 | 0 | 0.16795 | 0 |
| O (1) | 4i | 0.916 | 0.21627 | 0 | 0.27253 |
| O (2) | 8j | 1.855 | 0.21092 | 0.31094 | 0.23558 |

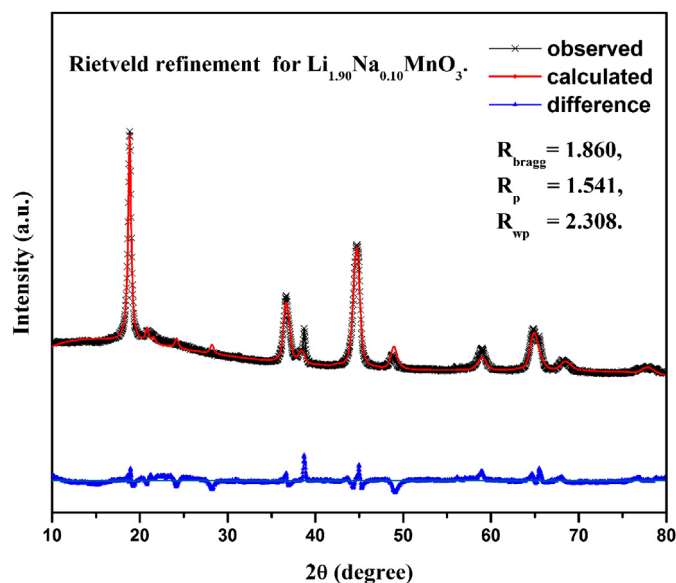


Fig. 16. Observed, calculated and difference plots for the X-ray Rietveld refinement of $\text{Li}_{1.90}\text{Na}_{0.10}\text{MnO}_3$.

4. Conclusions

Na-substituted Li_2MnO_3 , $\text{Li}_{1.90}\text{Na}_{0.10}\text{MnO}_3$, shows significant enhanced cycling stability compared with pristine Li_2MnO_3 . It delivers excellent discharge capacity retention of 99.3% after 45 cycles at $1/10 \text{ C}$ and 98.6% after 100 cycles at $1/2 \text{ C}$. The improved cycling performance can be attributed to the decrease of the grain size and the charge transfer resistance as well as the increase of the crystallinity and the Li-ion diffusion coefficient. Furthermore, a certain amount of spinel phase, which is induced by Na-substitution in the calcination process and cycle process, serves to facilitate Li-ion transport and stabilize the crystal structure.

Acknowledgement

The authors thank the National Natural Science Foundation of China (Grant no. 21203145) for financial support.

References

- [1] S.H. Park, Y. Sato, J.K. Kim, Y.S. Lee, Mater. Chem. Phys. 102 (2007) 225–230.
- [2] D.Y.W. Yu, K. Yanagida, Y. Kato, H. Nakamura, J. Electrochem. Soc. 156 (2009) A417–A424.
- [3] Z.H. Lu, J.R. Dahn, J. Electrochem. Soc. 149 (2002) A815–A822.
- [4] A.D. Robertson, P.G. Bruce, Chem. Commun. (2002) 2790–2791.
- [5] A.D. Robertson, P.G. Bruce, Chem. Mater. 15 (2003) 1984–1992.
- [6] S. Francis Amalraj, B. Markovsky, D. Sharon, M. Talianker, E. Zinigrad, R. Persky, O. Haik, J. Grinblat, J. Lampert, M. Schulz-Dobrick, A. Garsuch, L. Burlaka, D. Aurbach, Electrochim. Acta 78 (2012) 32–39.
- [7] P. Kalyani, S. Chitra, T. Mohan, S. Gopukumar, J. Power Sources 80 (1999) 103–106.
- [8] Y. Okamoto, J. Electrochem. Soc. 159 (2012) A152–A157.
- [9] V. Massarotti, D. Capsoni, M. Bini, G. Chiodelli, C.B. Azzoni, M.C. Mozziati, A. Paleari, J. Solid State Chem. 131 (1997) 94–100.
- [10] Y. Koyama, I. Tanaka, M. Nagao, R. Kanno, J. Power Sources 189 (2009) 798–801.
- [11] A.R. Armstrong, M. Holzapfel, P. Novak, C.S. Johnson, S.H. Kang, M.M. Thackeray, P.G. Bruce, J. Am. Chem. Soc. 128 (2006) 8694–8698.
- [12] J. Kikkawa, T. Akita, M. Tabuchi, K. Tatsumi, M. Kohyama, J. Electrochem. Soc. 158 (2011) A760–A768.
- [13] W.C. West, R.J. Staniewicz, C. Ma, J. Robak, J. Soler, M.C. Smart, B.V. Ratnakumar, J. Power Sources 196 (2011) 9696–9701.
- [14] S.H. Kim, S.J. Kim, K.S. Nahm, H.T. Chung, Y.S. Lee, J. Kim, J. Alloys Compd. 449 (2008) 339–342.
- [15] M. Tabuchi, Y. Nabeshima, T. Takeuchi, K. Tatsumi, J. Imaizumi, Y. Nitta, J. Power Sources 195 (2010) 834–844.
- [16] M. Tabuchi, Y. Nabeshima, T. Takeuchi, H. Kageyama, K. Tatsumi, J. Akimoto, H. Shibuya, J. Imaizumi, J. Power Sources 196 (2011) 3611–3622.

- [17] D. Mori, H. Sakaebe, M. Shikano, H. Kojitani, K. Tatsumi, Y. Inaguma, J. Power Sources 196 (2011) 6934–6938.
- [18] G. Singh, R. Thomas, A. Kumar, R.S. Katiyar, J. Electrochem. Soc. 159 (2012) A410–A420.
- [19] Z.L. Gong, H.S. Liu, X.J. Guo, Z.R. Zhang, Y. Yang, J. Power Sources 136 (2004) 139–144.
- [20] J. Breger, M. Jiang, N. Dupre, Y.S. Meng, Y. Shao-Horn, G. Ceder, C.P. Grey, J. Solid State Chem. 178 (2005) 2575–2585.
- [21] R. Xiao, H. Li, L. Chen, Chem. Mater. 24 (2012) 4242–4251.
- [22] Z. Li, J. Wang, S. Liu, X. Liu, S. Yang, J. Power Sources 196 (2011) 8160–8165.
- [23] C.S. Johnson, S.D. Korte, J.T. Vaughey, M.M. Thackeray, T.E. Bofinger, Y. Shao-Horn, S.A. Hackney, J. Power Sources 81 (1999) 491–495.
- [24] J.B. Goodenough, Y. Kim, Chem. Mater. 22 (2010) 587–603.
- [25] N. Yabuuchi, K. Yoshii, S.T. Myung, I. Nakai, S. Komaba, J. Am. Chem. Soc. 133 (2011) 4404–4419.
- [26] D. Shin, C. Wolverton, J.R. Croy, M. Balasubramanian, S.H. Kang, C.M.L. Rivera, M.M. Thackeray, J. Electrochem. Soc. 159 (2012) A121–A127.
- [27] M.M. Thackeray, Prog. Solid State Chem. 25 (1997) 1–71.
- [28] A.R. Armstrong, N. Dupre, A.J. Paterson, C.P. Grey, P.G. Bruce, Chem. Mater. 16 (2004) 3106–3118.
- [29] Z. Li, F. Du, X.F. Bie, D. Zhang, Y.M. Cai, X.R. Cui, C.Z. Wang, G. Chen, Y.J. Wei, J. Phys. Chem. C 114 (2010) 22751–22757.
- [30] R. Young Ho, K. Kanamura, J. Electrochem. Soc. 151 (2004) A1406–A1411.
- [31] L.L. Xiong, Y.L. Xu, C. Zhang, Z.W. Zhang, J.B. Li, J. Solid State Electrochem. 15 (2011) 1263–1269.
- [32] C.M. Julien, M. Massot, Mater. Sci. Eng., B 97 (2003) 217–230.
- [33] A. Abouimrane, O.C. Compton, H.X. Deng, I. Belharouak, D.A. Dikin, S.T. Nguyen, K. Amine, Electrochem. Solid State Lett. 14 (2011) A126–A129.
- [34] H. Bordeneuve, S. Guillemet-Fritsch, A. Rousset, S. Schuurman, V. Poulain, J. Solid State Chem. 182 (2009) 396–401.
- [35] B. Song, M.O. Lai, L. Lu, Electrochim. Acta 80 (2012) 187–195.
- [36] C.S. Johnson, N.C. Li, C. Lefief, J.T. Vaughey, M.M. Thackeray, Chem. Mater. 20 (2008) 6095–6106.
- [37] A. Ito, K. Shoda, Y. Sato, M. Hatano, H. Horie, Y. Ohsawa, J. Power Sources 196 (2011) 4785–4790.